

Frustrated spin correlations in diluted spin ice $\text{Ho}_{2-x}\text{La}_x\text{Ti}_2\text{O}_7$

G. Ehlers^{1,*}, E. Mamontov¹, M. Zamponi¹, J. S. Gardner^{2,3}, A. Faraone³, Y. Qiu³, A. L. Cornelius⁴, C. H. Booth⁵, K. C. Kam⁶, R. Le Toquin⁶ and A. K. Cheetham⁶

¹ *Spallation Neutron Source, Oak Ridge Nat. Lab., Bldg. 8600, Oak Ridge, TN 37831-6475, USA*

² *Indiana University, 2401 Milo B. Sampson Lane, Bloomington, Indiana 47408, USA*

³ *NIST Center for Neutron Research, NIST, Gaithersburg, MD 20899-8562, USA*

⁴ *Physics Dept., University of Nevada Las Vegas, Las Vegas, NV 89154-4002, USA*

⁵ *Chemical Sciences Division, Lawrence Berkeley National Laboratory, Berkeley, CA 94720, USA*

⁶ *Materials Research Laboratory, University of California, Santa Barbara, CA 93106, USA*

(version: February 4, 2008)

Abstract

We have studied the evolution of the static and dynamic spin correlations of spin ice $\text{Ho}_2\text{Ti}_2\text{O}_7$ where Ho was partially replaced by nonmagnetic La. Structural properties of diluted samples $\text{Ho}_{2-x}\text{La}_x\text{Ti}_2\text{O}_7$ were characterized by x-ray and neutron diffraction and by Ho L_{III} -edge and Ti K -edge extended x-ray absorption fine structure (EXAFS) measurements. It is found that the pyrochlore structure remains intact until about $x = 0.3$, but a systematic increase in local disorder with increasing La concentration is observed in the EXAFS data, especially from the Ti K edge. Quasielastic neutron scattering and a.c. susceptibility measurements show that, in $x \leq 0.4$ samples at temperatures above the macroscopic freezing, the spin-spin correlations are short ranged and dynamic in nature.

PACS: 75.40.Gb, 75.25.+z, 75.50.Dd, 71.27.+a, 74.70.Tx, 61.80.-x, 61.10.Ht

* Corresponding author, email: ehlersg@ornl.gov

Introduction

Over the last decade, the spin ices $\text{Dy}_2\text{Ti}_2\text{O}_7$ (DTO) and $\text{Ho}_2\text{Ti}_2\text{O}_7$ (HTO) have been established as topical materials in the context of frustrated magnetism [1, 2]. These systems provide a magnetic analogue to water ice with its residual entropy at low temperature caused by a macroscopic degeneracy of ground states and a particular freezing process [3].

The static spin correlations in the frozen ice state below $T \sim 1$ K have been characterized on a microscopic level by neutron diffraction [4] and reasonably well understood in terms of the dipolar spin ice model [5].

The dynamics of spin ice materials was first studied by a.c. susceptibility measurements which revealed a peak in the imaginary part $\chi''(\omega)$ in DTO at $T \sim 15$ K (i.e. well within the paramagnetic phase) that was initially not seen in HTO [6, 7]. In studies on diluted systems $\text{Dy}_{2-x}\text{Y}_x\text{Ti}_2\text{O}_7$ this peak was found to vanish with Y doping [8, 9] and then to re-emerge in very dilute systems [10]. Subsequently it was shown by neutron scattering that the peak is intrinsically also present in HTO [11]. All dynamical studies agreed in finding that the distribution of spin relaxation times remained very narrow on doping, and that no long range order was induced down to 100 mK [12, 13].

In this paper, we are interested in studying the evolution of the static and dynamic spin correlations of HTO when Ho is partially replaced by La. The main difference to an earlier study of the $(\text{Ho-Y})_2\text{Ti}_2\text{O}_7$ solid solution [13] is that the larger La^{3+} ion is expected to create significantly more strain and chemical pressure in the lattice than the Y^{3+} ion. Therefore a significant part of this paper is devoted to a characterization of the structural properties of the samples by means of different scattering techniques.

The crystalline symmetry of the pyrochlore phase $\text{A}_2\text{B}_2\text{O}_7$ depends mostly on the cationic ratio r_A/r_B . It has been shown that if this ratio is in the range $1.46 \leq r_A/r_B \leq 1.78$, the compound may adopt the cubic pyrochlore structure (space group $Fd\bar{3}m$) [14]. This structure is depicted in Fig. 1. While HTO is cubic with $r_A/r_B = 1.68$, pure $\text{La}_2\text{Ti}_2\text{O}_7$ (LTO) with $r_A/r_B = 1.92$ is known to crystallize in a monoclinic layered structure related to the perovskites (space group $P2_1$) [15].

Sample preparation and experimental techniques

Solid-solution samples with composition $\text{Ho}_{2-x}\text{La}_x\text{Ti}_2\text{O}_7$, $0 \leq x \leq 1.8$, were prepared by mixing Ho_2O_3 , La_2O_3 , and TiO_2 powders (Aldrich, 99.9%) in stoichiometric proportions. Each sample was heated up to 1400°C in air at 5°C min^{-1} for a period of four days with intermediate grindings. Powder x-ray diffraction was performed on Philips X'pert MPD diffractometer equipped with a 1D detector to increase the statistic. The data were analyzed by means of Rietveld refinement using the *Fullprof* software [16].

Samples with $x = 0, 0.1, 0.4$ and 1.7 were prepared for extended x-ray absorption fine structure (EXAFS) measurements by further grinding them in a mortar and pestle, passing them through a $20 \mu\text{m}$ sieve, brushing the resulting powder onto adhesive tape, and then stacking the tape to achieve a sample thickness t such that the change in the absorption μ at the edge corresponded to $\Delta\mu t \approx 1$. The samples were placed in a LHe-flow cryostat, and transmission data were recorded at the Ho L_{III} and the Ti K edges at $T = 30$ K. Data were collected on beam line 10-2 at the Stanford Synchrotron Radiation Laboratory, using a half-tuned Si(220) double monochromator. The data were analyzed using standard procedures [17]. In particular, the embedded atom absorption μ_0

was determined using a cubic spline with 5 knots over the data range, which was typically about 1 keV above the absorption threshold, E_0 , as determined by the position of the half-height of the absorption change at the edge. The data were fit in r -space using the RSXAP package [18] with theoretical scattering functions generated by FEFF7 [19].

Samples were then characterized by a.c. susceptibility measurements, in an external field up to 1 T, using commercially available fully calibrated magnetic measurement equipment. These measurements provide access to slow spin dynamics complementary to neutron scattering techniques.

Neutron diffraction was measured at room temperature at the BT-1 powder diffractometer at the NIST Center for Neutron Research. A wavelength of $\lambda = 1.54 \text{ \AA}$ was chosen from a Cu-(311) Bragg reflection. Quasielastic neutron time-of-flight (TOF) measurements were performed at the Disk Chopper Spectrometer (DCS) [20] at the NIST NCNR with an incident wavelength of 5.5 \AA (**Jason please verify**), giving an energy resolution of $\sim 20 \mu\text{eV}$ full width at half maximum (**Jason please verify**). The scattering patterns were appropriately corrected for sample transmission, background and detector efficiency using measurements of an empty container and a vanadium reference sample.

Neutron backscattering (BS) measurements were made at the new beam line 2 instrument at the Spallation Neutron Source (SNS) in Oak Ridge [21]. In backscattering one uses a polychromatic incident neutron beam and Si(111) analyzer crystals to select the final energy of $2082 \mu\text{eV}$ ($\lambda = 6.267 \text{ \AA}$) for scattered neutrons. At the elastic line the energy resolution was $\sim 3 \mu\text{eV}$. At the time of the experiments, SNS was running at 30 Hz, making a dynamic range of more than $\pm 400 \mu\text{eV}$ accessible. In these experiments, a vanadium reference sample was also measured. The neutron spin echo (NSE) [22] experiments were performed at the NSE spectrometer at the NIST NCNR using a neutron wavelength of $\lambda = 6 \text{ \AA}$ (bandwidth of 20%). This setting gives a Fourier time range of $40 \text{ ps} \leq t \leq 10 \text{ ns}$, over which correlations can be studied. Two values for the momentum transfer Q were chosen, $Q = 0.4 \text{ \AA}^{-1}$ and $Q = 0.7 \text{ \AA}^{-1}$. Instrumental resolution was measured with a $\text{Ho}_{0.7}\text{Y}_{1.3}\text{Ti}_2\text{O}_7$ sample, which is known to be static on the probed timescale at a temperature around or below $T \sim 5 \text{ K}$ [13].

Results - (a) x-ray and neutron diffraction

A neutron diffraction pattern of the $x = 0.1$ sample is shown in Fig. 2. The refined model parameters are summarized in table 1. The compounds with $x = 0.1$ and $x = 0.2$ were purely monophasic with the face centered cubic crystal structure (space group $Fd\bar{3}m$). Due to the larger ionic radius of La^{3+} , the cell parameter of the cubic cell increased from 10.1000 \AA for pure HTO to $10.1419(5) \text{ \AA}$ for $x = 0.2$. At further increasing La concentration, extra peaks corresponding to the LTO phase can be observed in the x-ray powder diffraction pattern. The samples essentially split into two co-existing phases, which are identified as La-doped HTO and Ho-doped LTO, respectively. The amount of LTO phase increases until x reaches a value of about 1.7, where only the LTO phase is present. Figure 3 shows that the sample separation into two phases depends linearly on the doping parameter x . In particular it is mentioned here that the $x = 0.4$ sample had a 10% content of the LTO phase. The cell parameter of the Ho-rich (HTO) phase is constant at around 10.1419 \AA throughout the biphasic region. As compared to pure HTO, the increase in cell parameter suggests that some amount of La goes into the Ho site until certain amount of strain is reached, where the cubic phase cannot accommodate any more La atoms (**site occupancies from x-rays**). Therefore, a cell parameter of 10.1419 \AA corresponds to the upper solubility limit of La in HTO. These results are thus quite similar to the $\text{Y}_{2-x}\text{La}_x\text{Ti}_2\text{O}_7$ series [23]. For completeness it is mentioned that

monoclinic LTO phase had refined cell parameter values of $a = 7.7657(12)$ Å, $b = 5.5136(9)$ Å, $c = 13.0013(24)$ Å and $\beta = 98.58(58)^\circ$ which were also constant throughout the bi-phasic region. From the diffraction results it was concluded that a study of the magnetic properties should be limited to the composition range $x \leq 0.4$.

Results - (b) EXAFS

The pyrochlore structure possesses a fairly straightforward local structure around the Ho and Ti sites, except that the 6 nearest-neighbor Ho-Ti (Ti-Ho) pairs are directly overlapping with the 6 nearest-neighbor Ho-Ho (Ti-Ti) pairs near 3.58 Å. The additional presence of La in the structure further complicates the fitting of this peak, so the same procedure was employed as in previous EXAFS studies of pyrochlores, [13, 24, 25] namely, for a given edge (*e.g.*, Ho L_{III}), the overlapping pairs near 3.58 Å (Ho-Ti, Ho-Ho and Ho-La) were constrained to the same pair separation distance, and the pair-distribution variances (σ^2) were constrained to the ratio of the reduced masses of the particular scatter pairs.

An additional constraint occurs because of the proximity of the La L_{III} edge to the Ti K edge. The Ti K edge (about 4965 eV) data range was limited to about 11.4 Å⁻¹ in samples with $x \neq 0$ by the presence of the La L_{III} edge at about 5483 eV. For such a short k -range, the correlation between the overall amplitude factor, S_0^2 , and the σ^2 parameters in the fit is expected to be very strong. S_0^2 was therefore obtained from fits to the $x = 0$ data using a wide (2.5-16 Å⁻¹) transform range, and then held fixed to this value for fits to the data from the other samples. A similar procedure was used for the Ho edge data, although only one transform range was required. It is noted that the overlap between the Ti and La edges even more severely limits the usability of the La L_{III} edge data, as the EXAFS oscillations from the underlying Ti K edge strongly interfere.

The data and fits for the pure material are shown in Fig. 4 and the fit parameters for all the data are summarized in Tables 2 and 3. Amplitude data for $x = 0, 0.1$ and 0.4 samples are shown in Fig. 5. Both the data and the fits for the $x = 1.7$ data indicate the sample is not close to a pure pyrochlore structure, and are not shown. Reported errors are from a Monte Carlo method assuming fit degrees of freedom can be obtained from Stern's rule [26]. R_{xrd} are x-ray diffraction results from Lian *et al.* [27].

The data and fit results for the pure Ho₂Ti₂O₇ material indicate a well ordered material. The Ho edge data and fits for the different samples are almost indistinguishable between the different samples, although the σ^2 parameter for the first Ho-O(1) peak increases notably for the $x=0.4$ data compared to the others, as does that for the Ho-Ti/Ho/La pairs. Interestingly, the Ti K -edge transforms are clearly different between the various samples, although this difference is not clearly indicated by the fit parameters. The σ^2 parameters for the first Ti-O(1) pairs do increase systematically, although not within the stated errors. The fit quality, however, gets noticeably worse with increasing x for the Ti edge data. Taken together, these data clearly indicate increasing disorder with x , especially for the $x = 0.4$ sample.

Results - (c) quasielastic neutron scattering, TOF

Fig. 6 shows the diffuse scattering observed at low temperature on a neutron time-of-flight spectrometer (DCS). The energy transfer was limited to ± 0.1 meV in the analysis. Again, one can see that the Bragg peaks for the $x = 1.7$ sample are at different positions than those of the samples

with $x \leq 0.4$ because the structure is different.

The diffuse scattering observed in the data is indicative of short ranged magnetic correlations known for the spin ices [28, 29]. One can identify two maxima in the magnetic $S(Q)$ around $Q \sim 0.6 \text{ \AA}^{-1}$ and $Q \sim 1.6 \text{ \AA}^{-1}$. At increasing x , the first maximum shifts slightly towards lower Q , which can be intuitively understood by the increased distance to nearest neighbors due to the additional voids. Within the energy resolution of the time-of-flight technique the diffuse scattering shown in Fig. 6 appears elastic at temperatures below $T \sim 50 \text{ K}$.

An analysis of the time-averaged spatial spin correlations was carried out by means of a reverse Monte Carlo (RMC) technique. A cube of $n \times n \times n$ cubic unit cells, $n = 6$, was considered with magnetic moments situated at the $16d$ sites. An appropriate amount of them was replaced by non-magnetic voids whose positions were chosen randomly. Individual moments were constrained to be parallel to a local $\langle 111 \rangle$ axis, to point to the center of a tetrahedron. Starting with an arbitrary spin configuration, a few spins were randomly chosen and flipped in one step of the simulation. A powder average of the cross section $d\sigma/d\Omega$ was then computed using

$$\frac{d\sigma}{d\Omega} = \text{const} \cdot F^2(Q) \cdot \sum_{m,n} \frac{\sin Qr_{m,n}}{Qr_{m,n}} \cdot \frac{\langle \mathbf{S}_m \cdot \mathbf{S}_n \rangle}{S(S+1)},$$

where m, n run through the cube, S denotes the moment on a site, $r_{m,n}$ is the distance between two sites, and $F(Q)$ is the magnetic form factor. The MC step was accepted if the fit to the measured intensity was improved, and repeated if not. The scale factor in the fit accounts for the fact that the measurement did not yield the scattering cross section in absolute units. Many individual MC runs were performed until convergence, and then linearly combined to produce the final best fit.

The fit to $d\sigma/d\Omega$ resulting from the reverse Monte Carlo simulation is also shown in the upper panel of Fig. 6, and the resulting time averaged spin correlations for near neighbor shells are shown in the lower panel. Even for nearest neighbors these correlations are very small, $\langle \mathbf{S}_m \cdot \mathbf{S}_n \rangle / S(S+1) \sim +0.07$ in the nearest neighbor shell. In the first neighbor shell the correlations are net ferromagnetic and in the next neighbor shells net antiferromagnetic. Overall the correlations are short ranged and do not extend beyond $\sim 10 \text{ \AA}$.

Results - (d) quasielastic neutron scattering, BSS and NSE

The data obtained with the high resolution scattering instruments – neutron backscattering and spin echo – show that the diffuse scattering is dynamic at temperatures $T > 1 \text{ K}$. These two techniques are complimentary in that backscattering measures neutron energy transfer $\hbar\omega$ while spin echo – as a Fourier technique – works in the time domain, but they also cover somewhat different (but overlapping) ranges in energy transfer (or Fourier time).

In the present study it is advantageous to combine these two techniques. As the data below shows, in the spin echo time window (starting at $40 \times 10^{-12} \text{ s}$) the information on the spin relaxation is incomplete as there is already some correlation lost at the shortest time. The backscattering data, covering (via Fourier transform) a time range shifted to somewhat shorter times, covers the initial drop in the NSE signal but carries no information of the relaxation function at the longer times.

Fig. 7 shows an example of the analysis of this data at $T = 100 \text{ K}$. NSE and BSS data were simultaneously fit to the same scattering law, a double exponential in time, which reads

$$\text{(NSE)} \quad \frac{I(Q, t)}{I(Q, 0)} = A \cdot e^{-t/\tau_1} + (1 - A) \cdot e^{-t/\tau_2}$$

$$\text{(BSS)} \quad S(Q, \omega) = I_{qel} \cdot \left\{ A \cdot \frac{\Gamma_1}{(\Gamma_1)^2 + (\hbar\omega)^2} + (1 - A) \cdot \frac{\Gamma_2}{(\Gamma_2)^2 + (\hbar\omega)^2} \right\} + I_{el} \cdot \delta(\omega)$$

where $\Gamma_{1,2} = \hbar/\tau_{1,2}$, I_{qel} is the quasielastic intensity, the factor I_{el} allows for nuclear incoherent elastic intensity (which NSE does not see), and the detailed balance factor has been omitted as $kT \gg \hbar\omega$. The NSE data is already corrected for instrumental resolution, while for the backscattering data the model function was convoluted with the instrumental resolution. In the analysis of backscattering data it is often observed that an instrument background term strongly correlates with fit parameters of the line width. This problem has been mitigated here by the very large dynamic range of the backscattering data, the very good signal/noise ratio, and by the correlation of the widths $\Gamma_{1,2}$ to the decay times in the NSE data.

It is intuitive to present the fit results in the time domain which is done in Fig. 8. One can see that the combination of both BSS and NSE data covers the full spin relaxation in the temperature range from 4 K to 150 K. The backscattering data also helped to confirm that the dynamics is independent of Q in the range from 0.3 \AA^{-1} to 2.0 \AA^{-1} . The relaxation times for the main relaxation process (index 2 above) compare very well to the results from pure spin ice (see next section) **ref**.

The main difference to the pure spin ice is the apparent presence of a second relaxation process at a shorter timescale which has a smaller weight in the scattering (for the $x = 0.4$ sample, $A \sim 0.2$ at 100 K). This can be ascribed to “defect assisted” relaxation of Ho spins in the pyrochlore lattice. Even though the $x = 0.4$ sample has a 10% contamination with a (potentially magnetic) monoclinic phase, the DCS data (Fig. 6) showed that this phase does *not* contribute to the diffuse scattering. This can be seen in Fig. 6 by a comparison of the intensities around 0.6 \AA^{-1} , noting that that the $x = 1.7$ sample is purely monoclinic while the $x = 0.4$ sample contains only 10%.

Results - (e) a.c. susceptibility

Bulk susceptibility measurements probe at much lower frequencies than neutron scattering, thus complementing the dynamic neutron experiments. Combined these two types of probes span 10 orders of magnitude in frequency. A gap from 10^4 to 10^8 remains open but when the results are combined like in Fig. 9 it appears that both techniques cover the same dynamical processes. Reports on a.c. susceptibility measurements on these and very similar systems have already been published **ref** which is why this section is kept short. The imaginary part of the a.c. susceptibility shows a main peak at a frequency dependent temperature. This is shown in the top left of Fig. 9. As discussed in the previous section, the neutron data also show one main relaxation mechanism whose frequency (inverse relaxation time from NSE) correlates with the measurement temperature as shown in the bottom right of Fig. 9. The neutron data roughly follow an Arrhenius law, i.e. thermal activation, with an activation energy $\Delta \sim 290$ K. In the vicinity of the freezing the temperature dependence is more complicated and not fully understood at the present time.

Summary and Conclusion

We have shown that in the $(\text{Ho-Y})_2\text{Ti}_2\text{O}_7$ system the pyrochlore structure survives up to a critical composition around $x = 0.3$. This is quite similar to the $\text{Y}_{2-x}\text{La}_x\text{Ti}_2\text{O}_7$ series [23]. At higher La concentration the samples are bi-phasic with coexisting Ho-rich pyrochlore and La-rich monoclinic phases. Ho L_{III} -edge and Ti K -edge extended EXAFS data give consistent results, showing increasing local disorder with x , especially for the $x = 0.4$ sample. The frustrated spin-spin correlations in HTO seem remarkably robust and little affected by the chemical alteration which creates magnetic voids in the lattice. This holds for both the time averaged correlations as well as the spin dynamics. To a small extent – although larger than in the $(\text{Ho-Y})_2\text{Ti}_2\text{O}_7$ system [13] – defect-assisted spin relaxation has been detected by high resolution neutron spectroscopy.

Acknowledgments

ORNL/SNS is managed by UT-Battelle, LLC, for the U.S. Department of Energy under contract DE-AC05-00OR22725. X-ray absorption data were collected at the Stanford Synchrotron Radiation Laboratory, a national user facility operated by Stanford University on behalf of the DOE/OBES. This work was supported by the U.S. Department of Energy under Contract No. DE-AC02-05CH11231. The authors are grateful for the local support staff at the NIST NCNR.

References

- [1] S. T. Bramwell and M. J. P. Gingras: *Science* **294**, 1495 (2001).
- [2] R. G. Melko and M. J. P. Gingras: *J. Phys: Condens. Matter* **16**, R1277 (2004).
- [3] A. P. Ramirez, A. Hayashi, R. J. Cava, R. Siddharthan, and B. S. Shastry: *Nature* **399**, 333 (1999).
- [4] S. T. Bramwell, M. J. Harris, B. C. den Hertog, M. J. P. Gingras, J. S. Gardner, D. F. McMorrow, A. R. Wildes, A. L. Cornelius, J. D. M. Champion, R. G. Melko, and T. Fennell, *Phys. Rev. Lett.* **87**, 047205 (2001).
- [5] B. C. den Hertog and M. J. P. Gingras, *Phys. Rev. Lett.*, **84**, 3430 (2000).
- [6] K. Matsuhira, Y. Hinatsu, K. Tenya, and T. Sakakibara, *J. Phys: Condens. Matter* **12**, L649 (2000).
- [7] K. Matsuhira, Y. Hinatsu, and T. Sakakibara, *J. Phys: Condens. Matter* **13**, L737 (2001).
- [8] J. Snyder, J. S. Slusky, R. J. Cava, and P. Schiffer, *Nature* **413**, 48 (2001).
- [9] J. Snyder, J. S. Slusky, R. J. Cava, and P. Schiffer, *Phys. Rev. B* **66**, 064432 (2002).
- [10] J. Snyder, B. G. Ueland, A. Mizel, J. S. Slusky, H. Karunadasa, R. J. Cava, and P. Schiffer, *Phys. Rev. B* **70**, 184431 (2004).
- [11] G. Ehlers, A. L. Cornelius, M. Orendáč, M. Kajňaková, T. Fennell, S. T. Bramwell, and J. S. Gardner: *J. Phys: Condens. Matter* **15**, L9 (2003).
- [12] M. Kajňaková, M. Orendáč, A. Orendáčová, A. Vlček, T. Fennell, and S. T. Bramwell, *J. Magn. Magn. Mater.* **272-276** e989 (2004).
- [13] G. Ehlers, J. S. Gardner, C. H. Booth, M. Daniel, K. C. Kam, A. K. Cheetham, D. Antonio, H. E. Brooks, A. L. Cornelius, S. T. Bramwell, J. Lago, W. Häussler, and N. Rosov, *Phys. Rev. B* **73**, 174429 (2006).
- [14] M. A. Subramanian, G. Aravamudan, and G. V. S. Rao, *Progress in Solid State Chemistry* **15** p. 55 (1983).
- [15] H. W. Schmalke, T. Williams, A. Reller, A. Linden, and J. G. Bednorz, *Acta Cryst. B* **49** 235 (1993).
- [16] J. Rodríguez-Carvajal, *Physica B: Condensed Matter* **192** 55 (1993).
- [17] G. G. Li, F. Bridges, and C. H. Booth, *Phys. Rev. B* **52**, 6332 (1995).
- [18] <http://lise.lbl.gov/R SXAP/>
- [19] A. L. Ankudinov and J. J. Rehr, *Phys. Rev. B* **56**, R1712 (1997).
- [20] J. R. D. Copley and J. C. Cook, *Chem. Phys* **292**, 477 (2003).
- [21] T. E. Mason et al., *Physica B* **385-386** 955 (2006).

- [22] G. Ehlers, *J. Phys: Condens. Matter* **18**, R231 (2006).
- [23] E. J. Harvey, S. E. Ashbrook, G. R. Lumpkin, and S. A. T. Redfern: *J. Mat. Chem.* **16** 4665 (2006).
- [24] C. H. Booth, E.-W. Scheidt, U. Killer, A. Weber, and S. Kehrein, *Phys. Rev. B* **66**, 140402(R) (2002).
- [25] S.-W. Han, J. S. Gardner, and C. H. Booth, *Phys. Rev. B* **69**, 024416 (2004).
- [26] E. A. Stern, *Phys. Rev. B* **48**, 9825 (1993).
- [27] Jie Lian, Jian Chen, L. M. Wang, Rodney C. Ewing, J. Matt Farmer, Lynn A. Boatner, and K. B. Helean, *Phys. Rev. B* **68**, 134107 (2003).
- [28] S. T. Bramwell, M. J. Harris, B. C. den Hertog, M. J. P. Gingras, J. S. Gardner, D. F. McMorrow, A. R. Wildes, A. L. Cornelius, J. D. M. Champion, R. G. Melko, and T. Fennell: *Phys. Rev. Lett.* **87**, 047205 (2001).
- [29] I. Mirebeau and I. Goncharenko: *J. Phys: Condens. Matter* **16**, S653 (2004).

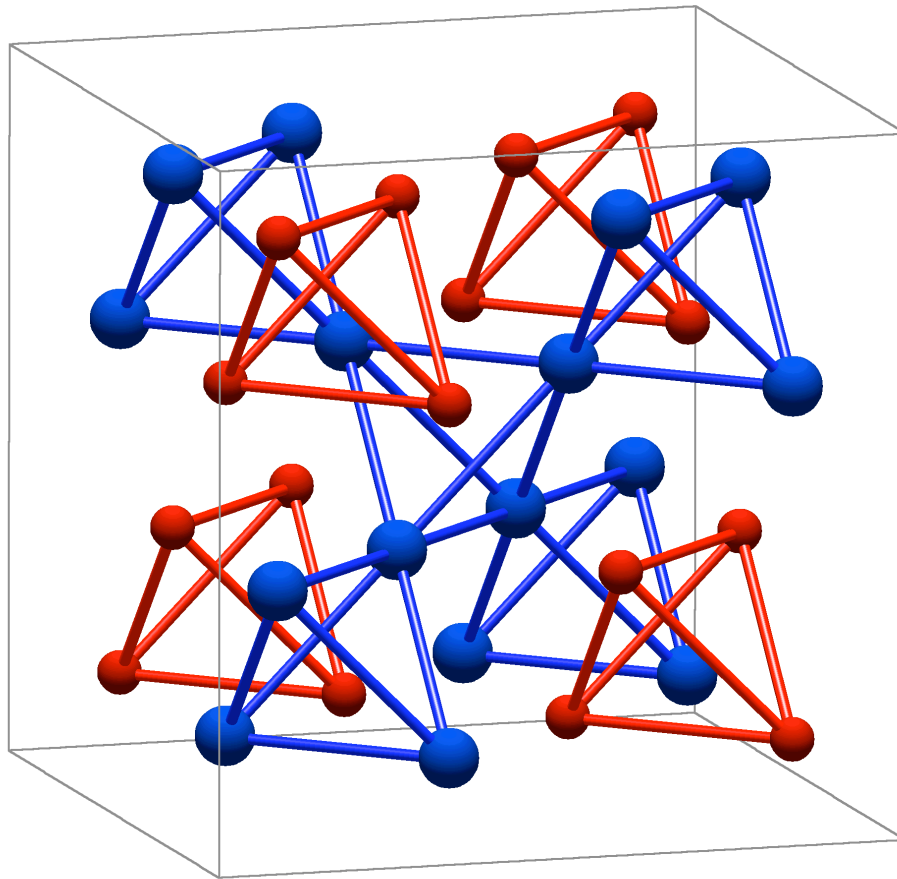


Figure 1: (Color online) A unit cell of the cubic pyrochlore structure showing the rare earth (blue) and titanium (red) sublattices.

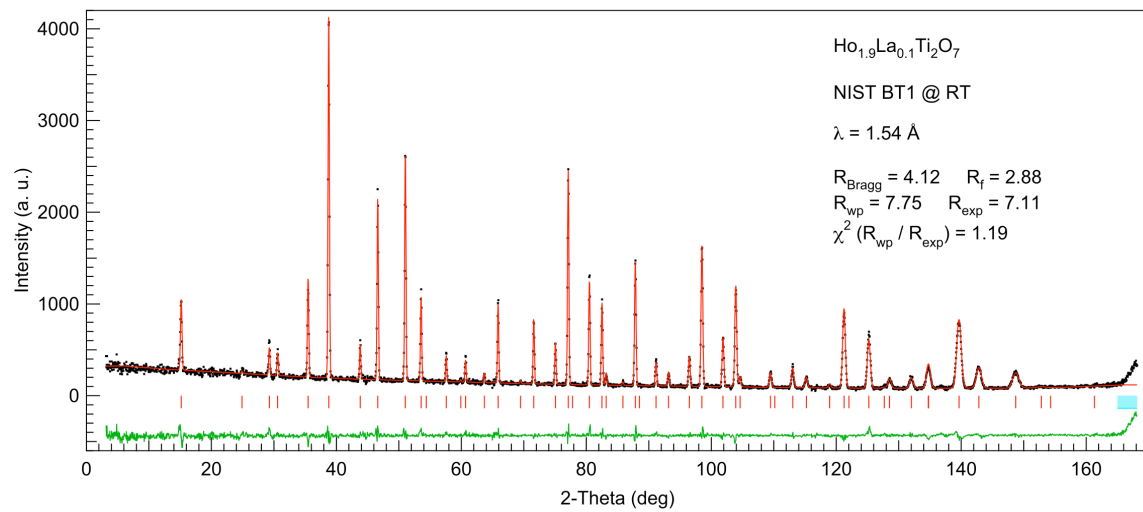


Figure 2: (Color online) Neutron powder diffraction pattern and Rietveld refinement of the $x = 0.1$ sample measured at room temperature. Shown are the observed counts, the calculated profile, and the difference. Bragg positions are marked by vertical ticks.

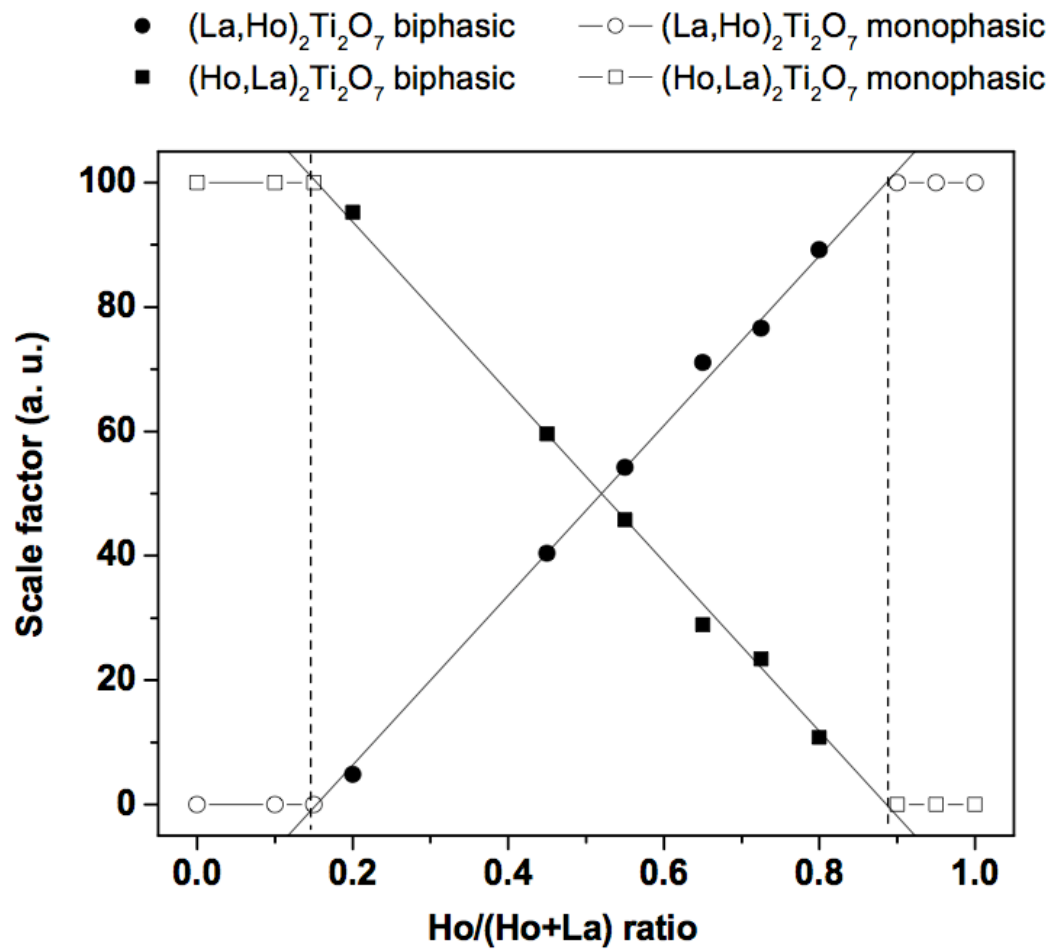


Figure 3: Evolution of the refined values of the scale factors of the pure HTO and LTO phases upon substitution from pure HTO phase to pure LTO phase. The sum of the two phases has been fixed to 100.

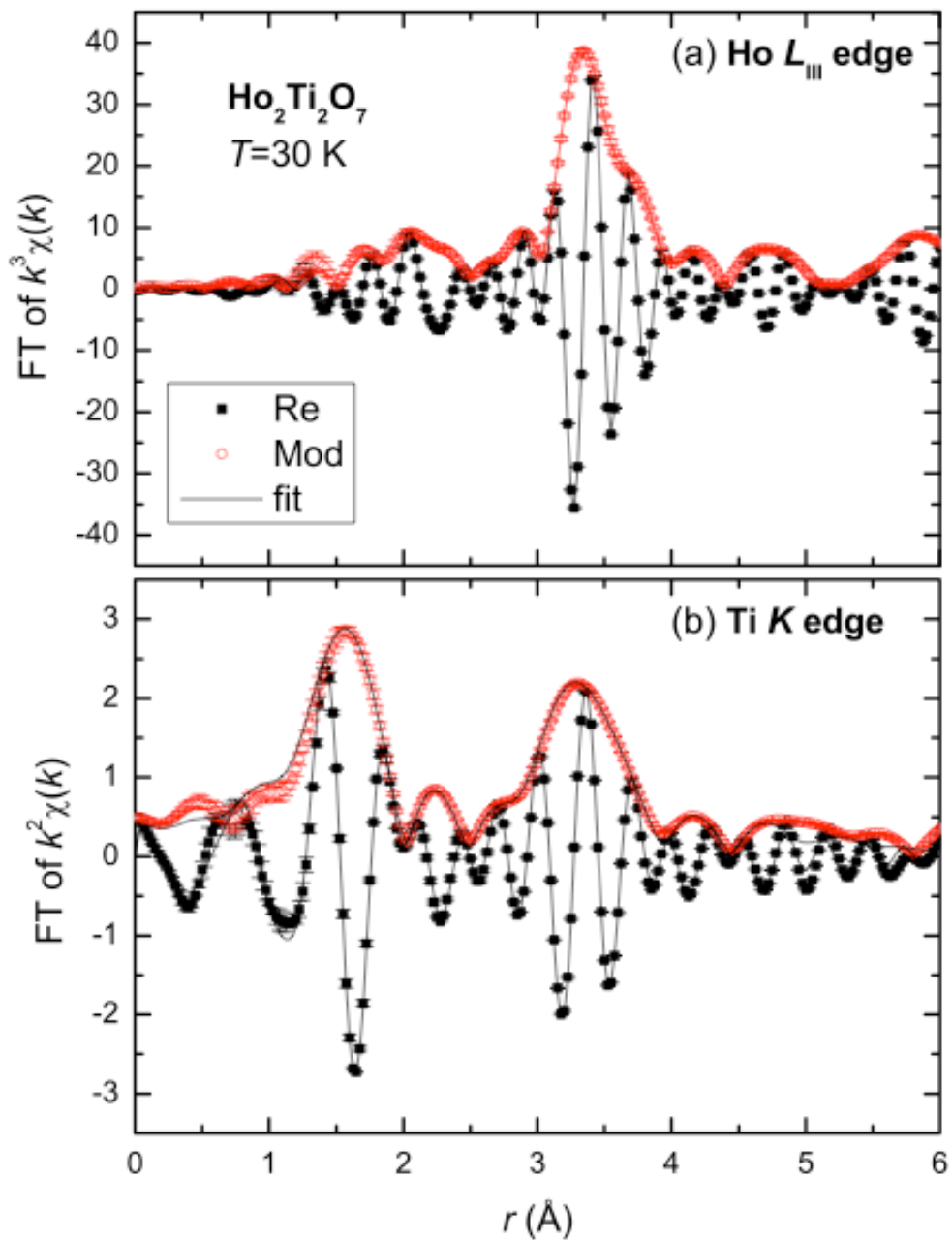


Figure 4: (Color online) (a) FT of the $k^3\chi(k)$ EXAFS data from the Ho L_{III} edge and (b) the FT of the $k^2\chi(k)$ of $T=30$ K data from the Ti K edge of pure $\text{Ho}_2\text{Ti}_2\text{O}_7$ are shown together with fits. Transform ranges are between 2.5 - 14.4 \AA^{-1} and 3.5 - 11.4 \AA^{-1} respectively, all Gaussian broadened by 0.3 \AA^{-1} . Error bars are based on the reproducibility over multiple scans.

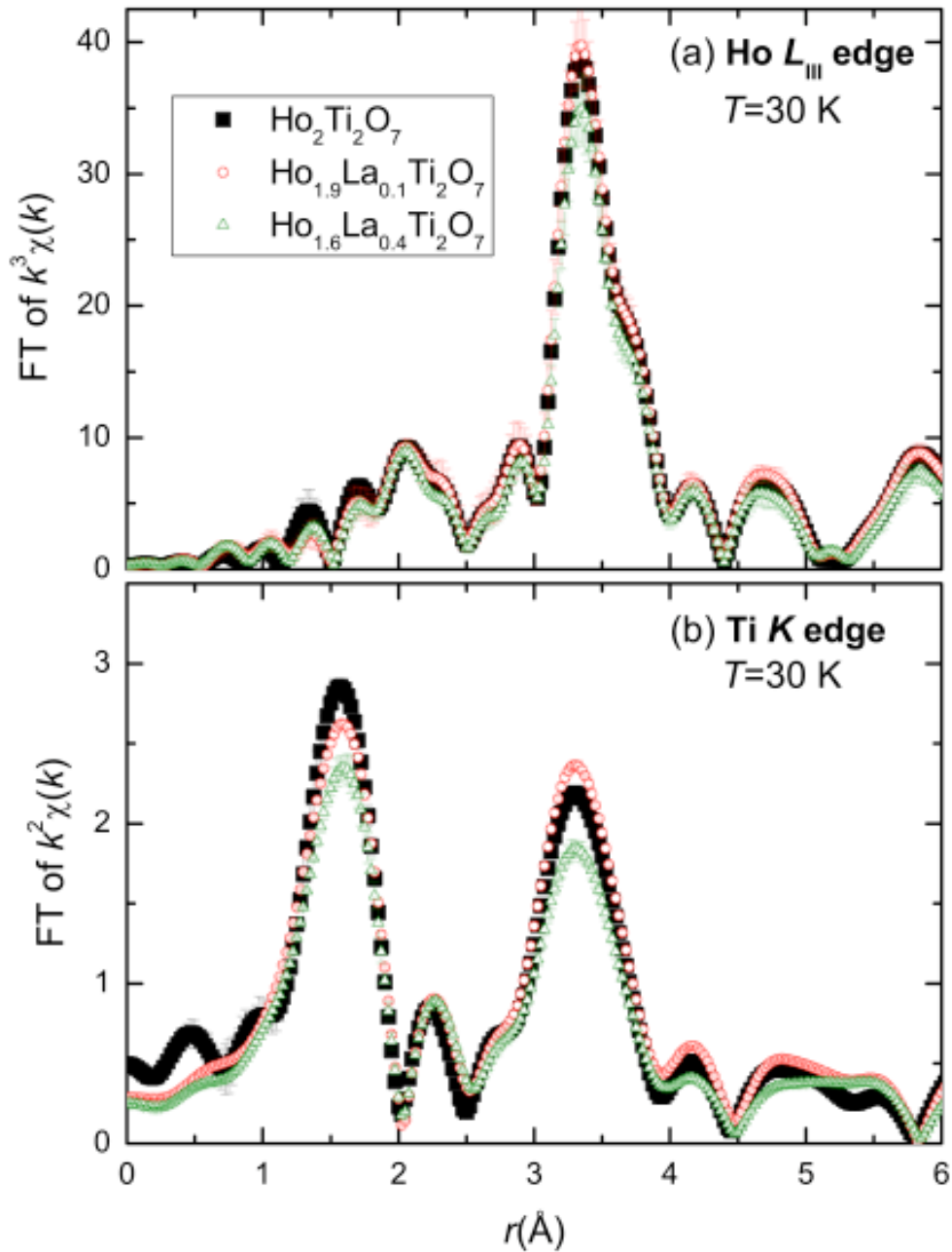


Figure 5: (Color online) (a) FT amplitudes of the $k^3\chi(k)$ EXAFS data from the Ho L_{III} edge and (b) the FT of the $k^2\chi(k)$ of data from the Ti K edge for the $x=0, 0.1$ and 0.4 samples, all at $T=30$ K. Transform ranges are as in Fig. 4.

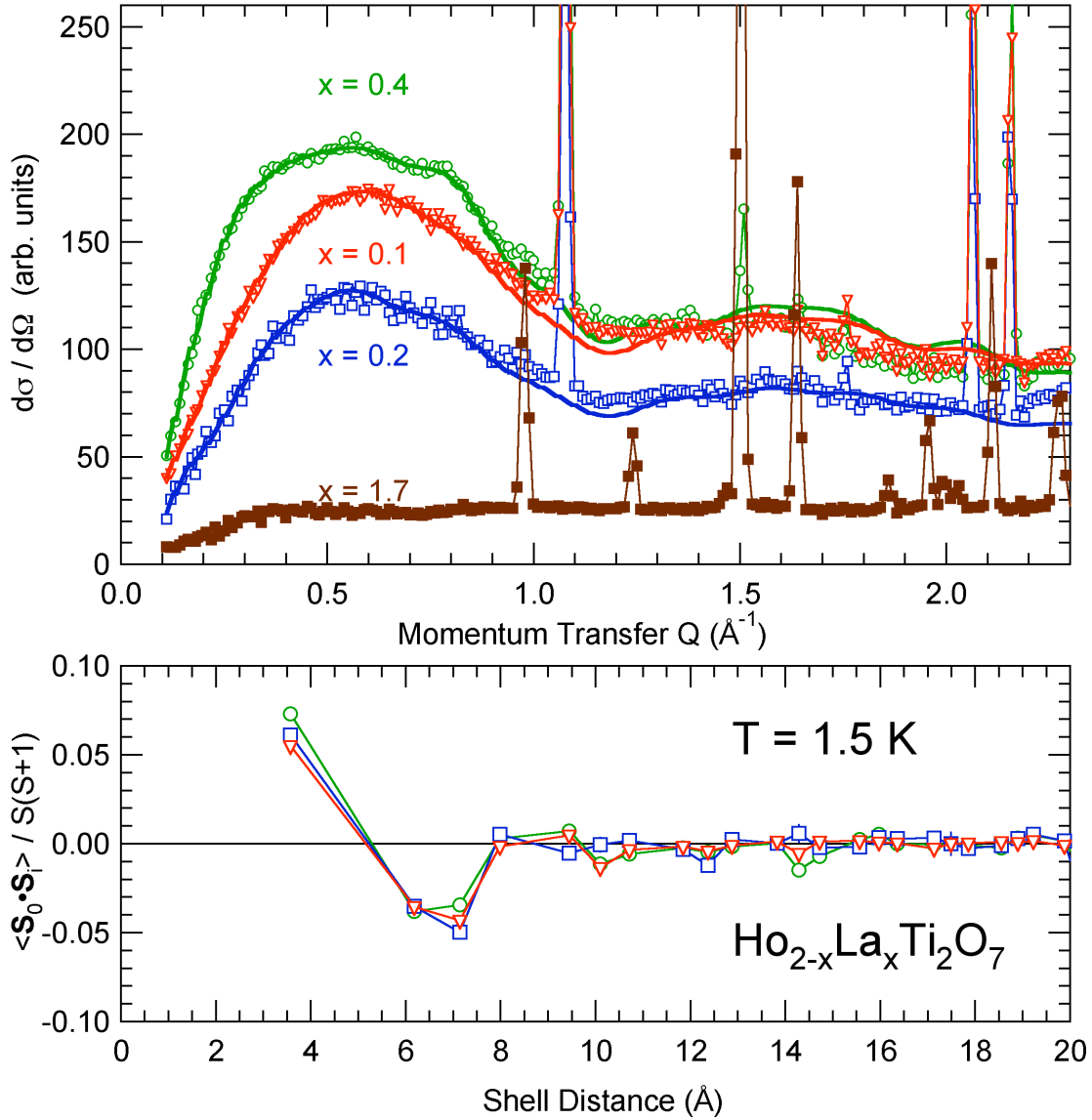


Figure 6: (Color online) Diffuse magnetic scattering studied at DCS, corrected for Vanadium and monitor intensities. The energy window was set to ± 0.1 meV. Intensity is highest at $x=0.4$ because of sample transmission. One can see first and second maxima of the diffuse $S(Q)$. The lower panel shows the spin correlation in the near neighbor shells.

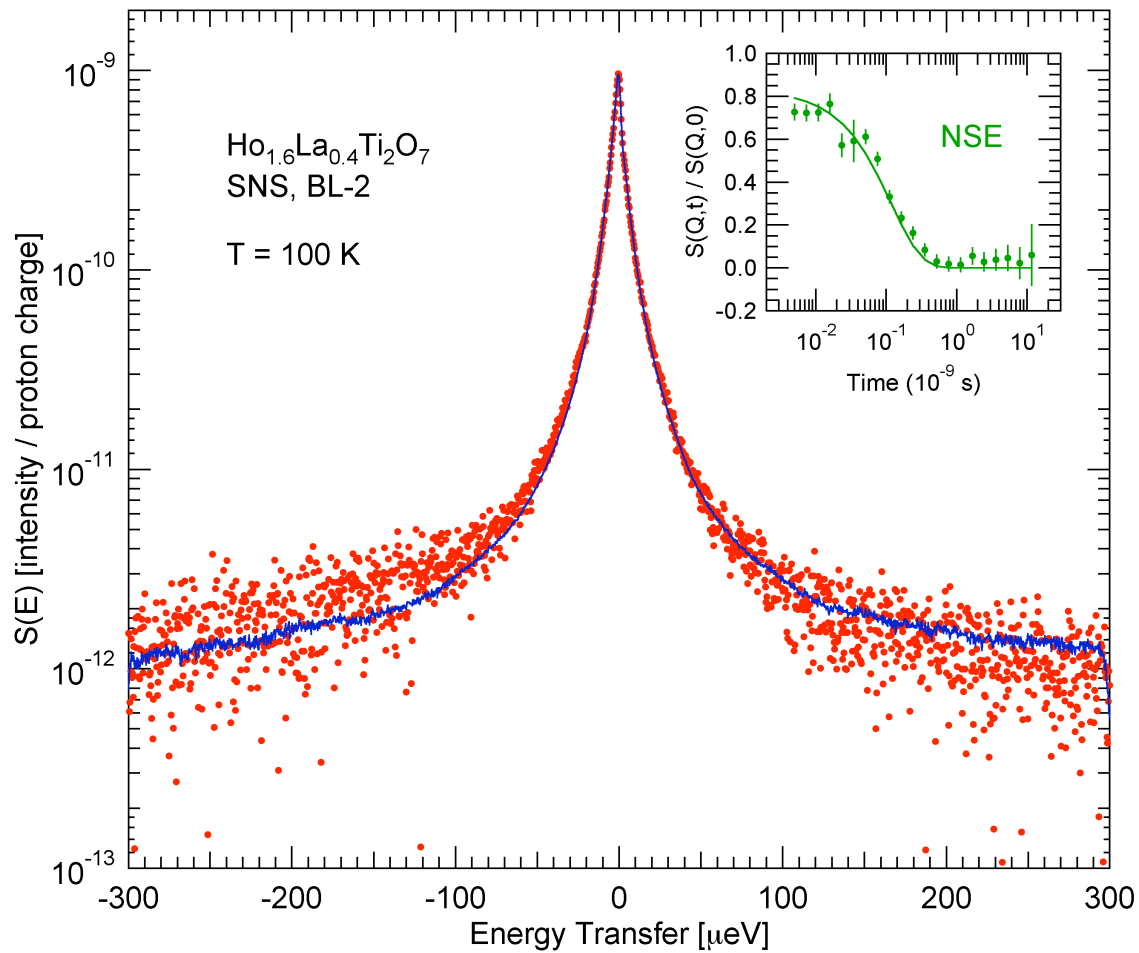


Figure 7: (Color online) NSE and BSS data and fits combined at $T = 100$ K for the $x = 0.4$ sample.

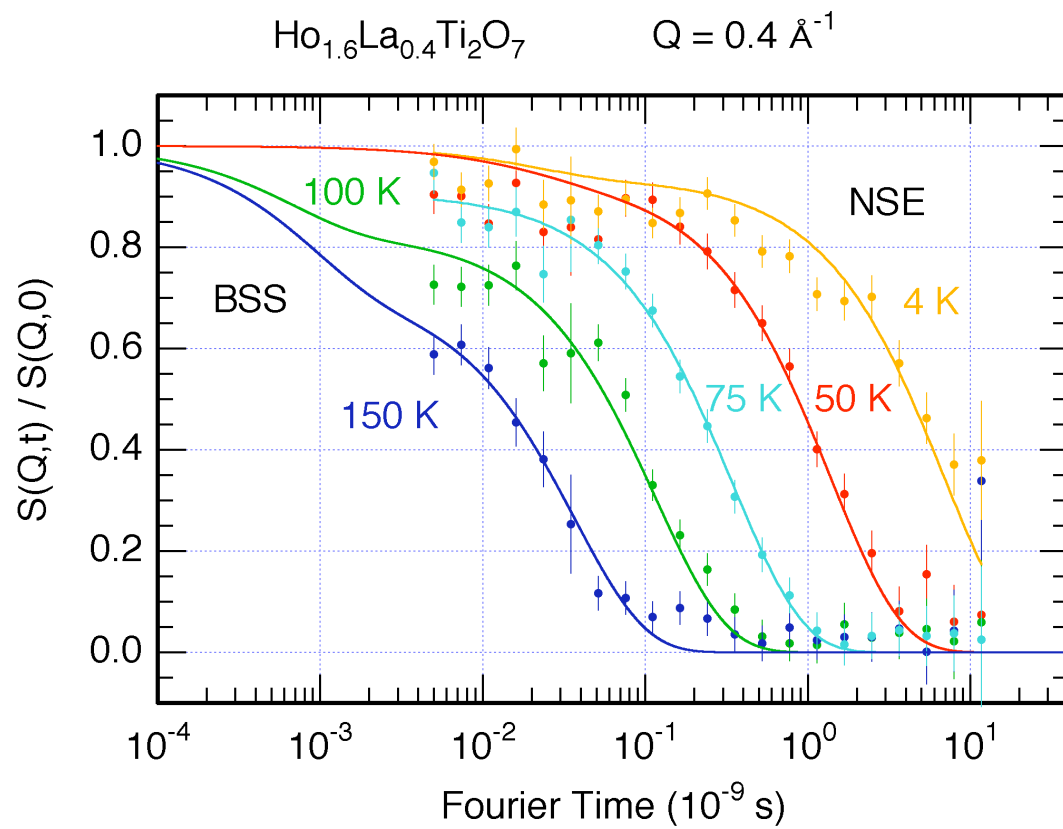


Figure 8: (Color online) The spin correlation functions and fits from NSE and BSS data shown in the time domain.

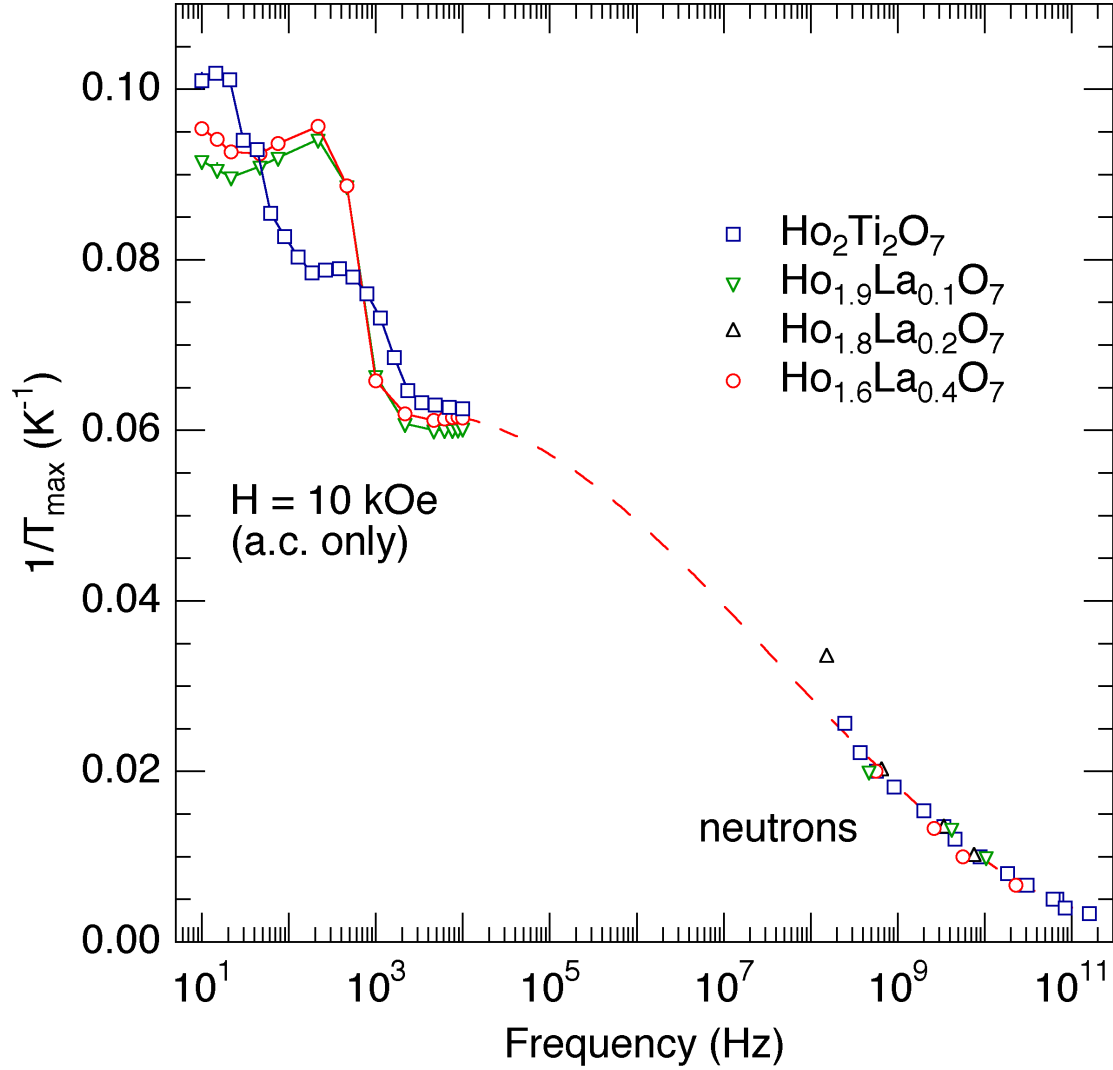


Figure 9: (Color online) Combination of results from a.c. susceptibility (top left) and quasielastic neutron scattering (bottom right) measurements. For susceptibility, this graph shows the inverse of the temperatures at which maxima in the imaginary part occur, as a function of the probing frequency, for the $x = 0$, $x = 0.1$ and $x = 0.4$ samples. For the neutron data, the inverse measurement temperature is plotted against the inverse of the spin relaxation time as fitted from either NSE or backscattering. Symbols used: $x = 0$ (\square), $x = 0.1$ (∇), $x = 0.2$ (\triangle), $x = 0.4$ (\circ). The slope of the curve of the NSE data corresponds to $\Delta \sim 290$ K.

Compound	Ho _{1.9} La _{0.1} Ti ₂ O ₇				
<i>Position</i>	Atom	Occ.	ideal Occ.	x, y, z	β_{iso}
16 <i>d</i>	Ho	0.0792	0.0792	$\frac{1}{2}, \frac{1}{2}, \frac{1}{2}$	0.3
16 <i>d</i>	La	0.0041	0.0041	$\frac{1}{2}, \frac{1}{2}, \frac{1}{2}$	0.3
16 <i>c</i>	Ti	0.0833	0.0833	0, 0, 0	0.3
48 <i>f</i>	O	0.255(1)	0.250	$0.3284(1), \frac{1}{8}, \frac{1}{8}$	0.53(1)
8 <i>b</i>	O	0.043(0)	0.0417	$\frac{3}{8}, \frac{3}{8}, \frac{3}{8}$	0.53(1)
Symmetry	$Fd\bar{3}m$				
a	10.1182(1) Å				

Table 1: Refinement results from neutron diffraction for the Ho_{1.9}La_{0.1}Ti₂O₇ sample. Isotropic displacement factors were refined only for the oxygen sites.

	$x=0.0$				$x=0.1$			$x=0.4$		
	N	$\sigma^2(\text{Å}^2)$	$R(\text{Å})$	R_{xrd}	N	$\sigma^2(\text{Å}^2)$	$R(\text{Å})$	N	$\sigma^2(\text{Å}^2)$	$R(\text{Å})$
Ho-O(2)	2	0.0020(5)	2.189(5)	2.188	2	0.0028(4)	2.185(3)	2	0.0025(2)	2.187(2)
Ho-O(1)	6	0.0059(5)	2.471(4)	2.489	6	0.0056(2)	2.478(2)	6	0.0066(1)	2.480(1)
Ho-Ti	6	0.0039(6)	3.576(1)	3.572	6	0.0037(1)	3.580(2)	6	0.0047(1)	3.587(1)
Ho-Ho	6	0.0018	3.576	3.572	5.7	0.0017	3.580	4.8	0.0021	3.587
Ho-La	-	-	-	-	0.3	0.0018	3.580	1.2	0.0023	3.587
Ho-O(1)	12	0.009(1)	4.01(1)	4.072	12	0.008(1)	4.015(6)	12	0.0078(7)	4.044(5)
ΔE_0		-7.0(9)							-7.5(3)	
S_0^2		1.03(6)				1.03			1.03	
$R(\%)$		3.87				3.90			2.72	

Table 2: Ho_{2-x}La_xTi₂O₇ fit results from Ho L_{III} -edge data at 30 K. Fit range is between 1.50 and 4.00 Å. The k^3 -weighted data are transformed between 2.50-14.30 Å⁻¹ and are Gaussian narrowed by 0.30 Å⁻¹. Multiple scattering was included in the fits, but the results for those peaks are not shown. Absolute errors are typically 0.005 Å in R and 10% in σ^2 for the nearest neighbors, and double for the further neighbors.

	$x=0.0, k_{\max}=16.0 \text{ \AA}^{-1}$				$x=0.0$			$x=0.1$			$x=0.4$		
	N	$\sigma^2(\text{\AA}^2)$	$R(\text{\AA})$	$R_{\text{xrd}}(\text{\AA})$	N	$\sigma^2(\text{\AA}^2)$	$R(\text{\AA})$	N	$\sigma^2(\text{\AA}^2)$	$R(\text{\AA})$	N	$\sigma^2(\text{\AA}^2)$	$R(\text{\AA})$
Ti-O(1)	6	0.0021(4)	1.964(5)	1.954	6	0.0023(3)	1.964(6)	6	0.0026(5)	1.96(1)	6	0.0033(9)	1.96(1)
Ti-Ti	6	0.0037(3)	3.560(3)	3.572	6	0.0031(4)	3.550(7)	6	0.0021(6)	3.58(1)	6	0.0035(8)	3.63(1)
Ti-Ho	6	0.0024	3.560	3.572	6	0.0020	3.550	5.7	0.0014	3.58	4.8	0.0022	3.63
Ti-La	-	-	-	-	-	-	-	0.3	0.0014	3.58	1.2	0.0023	3.63
Ti-O(1)	6	0.006(4)	3.74(1)	3.769	6	0.008(4)	3.71(1)	6	0.001(2)	3.76(3)	6	0.00(1)	3.83(2)
Ti-O(2)	6	0.006	6	4.16	4.189	0.008	4.13	6	0.001	4.19	6	0.00	4.245
Ti-O(1)	12	0.006	12	4.32	4.354	0.008	4.29	12	0.001	4.36	12	0.00	4.410
$\Delta E_{0,1}$		1(1)				1(1)				2(3)		1(4)	
ΔE_0		8(1)				2(1)				4(4)		-4(3)	
S_0^2		0.89(6)				0.89				0.89		0.89	
$R(\%)$		9.88				6.07				9.38		17.86	

Table 3: $\text{Ho}_{2-x}\text{La}_x\text{Ti}_2\text{O}_7$ fit results from Ti K -edge data at 30 K. Fit range is between 1.40 and 4.60 \AA . For most fits, the k^2 -weighted data are transformed between 3.5-11.4 \AA^{-1} and are Gaussian narrowed by 0.30 \AA^{-1} . The overall scale factor S_0^2 is obtained from fits to the $x=0$ data that extend to 16.0 \AA^{-1} . These fits also required a separate ΔE_0 for the first scatter pair, Ti-O(1). Multiple scattering was included in the fits, but the results for those peaks are not shown. Absolute errors are typically 0.005 \AA in R and 10% in σ^2 for the nearest neighbors, and double for the further neighbors.